

# The INTOA Experiment: A Study of Ocean-Atmosphere Interactions Under Moderate to Strong Offshore Winds and Opposing Swell Conditions in the Gulf of Tehuantepec, Mexico

F. J. Ocampo-Torres · H. García-Nava · R. Durazo ·  
P. Osuna · G. M. Díaz Méndez · H. C. Graber

Received: 18 June 2010 / Accepted: 26 October 2010 / Published online: 13 November 2010  
© Springer Science+Business Media B.V. 2010

**Abstract** The Gulf of Tehuantepec air–sea interaction experiment (INTOA) took place from February to April 2005, under the Programme for the Study of the Gulf of Tehuantepec (PEGoT, Spanish acronym for Programa para el Estudio del Golfo de Tehuantepec). PEGoT is underway aiming for better knowledge of the effect of strong and persistent offshore winds on coastal waters and their natural resources, as well as performing advanced numerical modelling of the wave and surface current fields. One of the goals of the INTOA experiment is to improve our knowledge on air–sea interaction processes with particular emphasis on the effect of surface waves on the momentum flux for the characteristic and unique conditions that occur when strong *Tehuano* winds blow offshore against the Pacific Ocean long period swell. For the field campaign, an air–sea interaction spar (ASIS) buoy was deployed in the Gulf of Tehuantepec to measure surface waves and the momentum flux between the ocean and the atmosphere. High frequency radar systems (phase array type) were in operation from two coastal sites and three acoustic Doppler current profilers were deployed near-shore. Synthetic aperture radar images were also acquired as part of the remote sensing component of the experiment. The present paper provides the main results on the wave and wind fields, addressing the direct calculation of the momentum flux and the drag coefficient, and gives an overview of the INTOA experiment. Although the effect of swell has been described in recent studies, this is the first time for the very specific conditions encountered, such as swell persistently opposing offshore winds and locally generated waves, to show a clear evidence of the influence on the wind stress of the significant steepness of swell waves.

---

F. J. Ocampo-Torres (✉) · H. García-Nava · P. Osuna  
Departamento de Oceanografía Física, CICESE, Ensenada, BC, México  
e-mail: ocampo@cicese.mx

R. Durazo · G. M. Díaz Méndez  
Facultad de Ciencias Marinas, Universidad Autónoma de Baja California, Ensenada, BC, México

H. C. Graber  
Rosenstiel School of Marine and Atmospheric Science, University of Miami, Miami, FL, USA

**Keywords** Air–sea interaction · Field measurements · INTOA · Momentum flux · Sea state

## 1 Introduction

Momentum exchange between the atmosphere and ocean, together with the vertical fluxes of heat and moisture, play a fundamental role on weather and climate, and their variability over a wide range of time and space scales. Knowledge on how wind stress varies with environmental parameters is of increasing importance, especially for the modelling of air–sea interaction for ocean current and wave prediction. A good number of recent experiments and field campaigns have been carried out to better understand the fundamental processes related to air–sea interaction and the underlying physics of various phenomena influencing directly the atmospheric boundary layer or the ocean mixed layer: *Flux, etat de la mer, et télédétection en conditions de fetch variable* FETCH (Hauser et al. 2003); the southern ocean waves experiment, SOWEX (Banner et al. 1999); *Couplage avec l'Atmosphère en Conditions Hivernales*/The Fronts and Atlantic Storm-Track Experiment, CATCH/FASTEX (Eymard et al. 1999); just to mention a few. All these experiments have yielded important contributions to the understanding of air–sea transfer processes, however, there are still open questions. In particular, the influence of the sea state and underlying swell on the air–sea interaction requires further study to adequately understand fundamental processes.

In this context, the Gulf of Tehuantepec air–sea interaction INTOA experiment was organised and carried out, where moderate to strong winds show a persistent southerly direction (*Tehuano* events), while long period swell travels to the study region and propagates there practically northwards. The *Tehuano* events are stronger and more common during the winter (Romero-Centeno et al. 2003). The study area can easily be considered as a natural laboratory where specific research dealing with the interaction of locally generated wind-sea and opposing swell is very appealing. Furthermore, the analysis of the wave-field evolution under fetch-limited conditions is also of great interest in this particular region.

The INTOA experiment is one component of the PEGoT (Spanish acronym for Programa para el Estudio del Golfo de Tehuantepec) programme. PEGoT is underway aiming for a better knowledge of the effect of *Tehuano* events (strong and persistent offshore winds) on coastal waters and their natural resources, as well as performing advanced numerical modelling of the wave and surface current fields. Under the PEGoT programme various research projects are being carried out, dealing with the determination of the influence of *Tehuano* events on the surface circulation as inferred through measurements obtained with high frequency radar systems, as well as analysing the genesis of oceanic eddies and their interaction with the larger scale circulation in the Tropical Pacific Mexican waters.

The INTOA experiment's main objectives are: (1) to improve our knowledge of air–sea interaction processes with particular emphasis on the effect of surface waves on the momentum flux in the characteristic local conditions that occur in the Gulf of Tehuantepec (strong *Tehuano* winds blowing offshore against the Pacific Ocean long period swell); (2) to describe the dependence of momentum flux on environmental conditions, such as sea state, ocean swell, wind field and ocean surface currents; (3) to determine the swell evolution in coastal waters under the influence of the locally generated wind-sea in the opposite direction, with emphasis on swell attenuation; (4) to characterise the influence of *Tehuano* events as a forcing mechanism on surface currents; and (5) to test wind, wave, and surface current retrieval algorithms currently applied to remote sensing information as obtained by synthetic aperture and high frequency radar systems.

Closely linked to main objectives (1) and (2) mentioned above, the purpose of this paper is to describe the wave field evolution and wind conditions, specifically addressing the direct calculation of momentum fluxes. Evidence of the influence of swell significant steepness on the directly estimated wind stress is presented. We also provide some background and the goals of PEGoT, and the main objectives of the air–sea interaction component, the set-up for the INTOA experiment and field campaign, and an overview of the dominant oceanic and atmospheric conditions (see, for instance, [García-Nava et al. \(2009\)](#) for further information on the scientific objectives).

Preliminary results on the remote sensing component of the experiment are briefly shown. However, those other aspects such as the high frequency (HF) radar system detailed description and results, and further analysis of advanced synthetic aperture radar (ASAR) images to provide quantitative information on wind fields and the spatial evolution of swell, are omitted herein but will be considered in a subsequent contribution.

In the following section a description of the INTOA Experiment is provided. The main results follow, explaining the overall mean conditions, wind and waves characteristics encountered, and some relevant aspects of the momentum flux and the drag coefficient as calculated directly from the measurements. Some conclusions are delivered in the last section.

## 2 Field Campaign

The INTOA experiment measurement campaign was carried out from February to April 2005 in the Gulf of Tehuantepec (Fig. 1). Momentum flux, wave field, and other related atmospheric and oceanic variables were measured directly and simultaneously from a moored air–sea interaction spar (ASIS) buoy. The location was selected to monitor air–sea interaction variables under fetch limited conditions during *Tehuano* events. The ASIS buoy is a stable platform especially designed for air–sea interaction studies, and produces very low distortion of the surface and air flow ([Graber et al. 2000](#)). For the INTOA experiment the ASIS buoy was attached to a tether buoy by a surface floating line of about 40 m long, and was deployed from the DR06 Bahía Tepoca dredge vessel of the Mexican Navy (Secretaría de Marina-Armada de México) and moored from 22 February to 24 April 2005 in the central part of the Gulf of Tehuantepec at 16° N and 95° W, approximately 22 km offshore at a 60-m depth location (Fig. 1).

A list of the sensors on the ASIS buoy and some of their characteristics are detailed in Table 1. The three turbulent components of the wind velocity were recorded with a sonic anemometer sampling at 20 Hz and located at about 6.5 m above mean sea level. Sea-surface elevation was also sampled at 20 Hz by an array of six wave gauges continuously measuring capacitance. The buoy motion was detected and recorded at the same sampling rate through the measurements of three linear accelerometers, three clinometers and a compass, providing the six components of motion of the buoy. Air temperature, humidity and atmospheric pressure were sampled at 1 Hz. Sub-surface water temperature was measured every 5 s at the ASIS buoy while sub-surface current measurements were obtained every 10 min below the tether buoy. Recording the buoy motion is crucial in order to correct all other measurements by referring them to a proper coordinate system following available algorithms ([Ancitil et al. 1994](#); [Drennan et al. 1994](#)). Data acquired during 30-min runs were used to calculate the momentum flux through the eddy-correlation method, the directional wave spectra, and averages and other integral variables reported herein, such as significant wave height  $H_S$ , wave direction associated with the spectral peak  $\theta$ , mean wind speed  $U$  and direction  $\theta_U$ . Directional wave spectra were calculated using the maximum likelihood

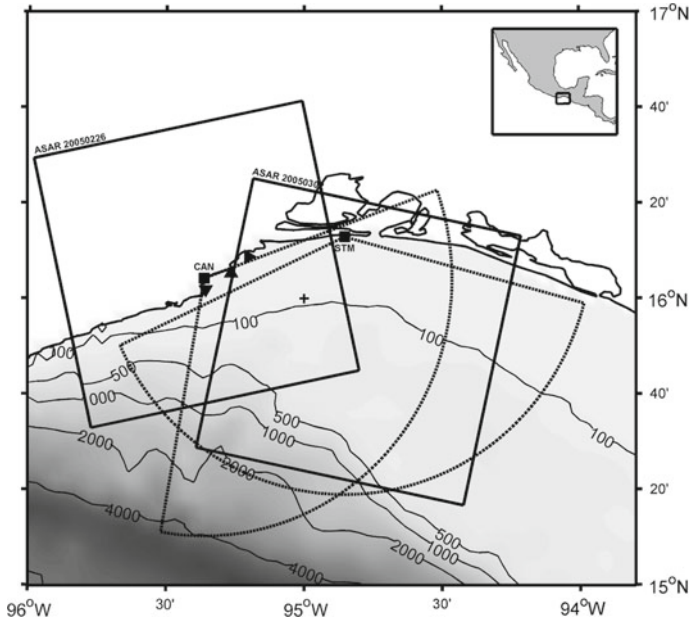


**Fig. 1** Map of the Gulf of Tehuantepec study area with grey-shaded bathymetry (depth contours in m). The *black square* frames represent the area covered by two ASAR images acquired respectively on 26 February 2005 at 0420 UTC and 2 March 2005 at 1620 UTC. Some wave-field characteristics estimated from this type of image are shown in Fig. 6. Mooring location for the ASIS buoy is also shown (*plus sign*). HF radar WERA system sites (*squares*) and coverage (*dotted*) are shown for Santa María del Mar (STM) and Cangrejo (CAN) stations. Locations for near-shore deployed Nortek acoustic Doppler current profilers are for Espigon station (*triangle pointing East*), Castillo station (*triangle pointing North*), and Chipehua station (*triangle pointing West*). The *inset* shows the study area location within the Pacific coast of Mexico

**Table 1** List of sensors and some of their characteristics used onboard the ASIS buoy for the INTOA field campaign in the Gulf of Tehuantepec during the first part of 2005

Sensor	Brand	Model	Sampling frequency	Height (m)
Sonic anemometer	Gill	R3A	20 Hz	6.5
Capacitance wave gauges	CCIW <sup>a</sup>		20 Hz	±1.25
Linear accelerometer	Columbia Res. Lab.	SA-307HPTX	20 Hz	-7
Clinometers	Systron Donner In. Div.	GC1-00050-100	20 Hz	-7
Compass	Precision Navigation Inc.	TCM-2	1 Hz	-7
Temperature and humidity probe	Jautering Int. Corp.	MP101A	1 Hz	4.5
Barometer	Setra	270	1 Hz	2.5
Thermistor	Richard Brancker Res.	TR-1050P	0.2 Hz	-2.5
Current meter	General Oceanics Inc.	UCM-600L	5 Cyc h <sup>-1</sup>	-6

<sup>a</sup> Canada Centre for Inland Waters

method, as described in [Drennan et al. \(1994\)](#), when reliable information from at least four wave staffs was available. The installation of the ASIS buoy during the INTOA experiment represents the first time a platform of this type is deployed successfully in Latin-American waters.

Directional wave measurements and the current profile were acquired with acoustic Doppler current profilers (Nortek, Aquadopp) deployed near-shore at three locations (triangles in [Fig. 1](#)) where the water depth is about 20 m: (1) Espigón station at  $16^{\circ}8.74' \text{ N}$  and  $95^{\circ}12.13' \text{ W}$ , (2) Castillo station at  $16^{\circ}5.3' \text{ N}$  and  $95^{\circ}15.9' \text{ W}$ , and (3) Chipehua station at  $16^{\circ}1.89' \text{ N}$  and  $95^{\circ}21.39' \text{ W}$ . Surface elevation-induced pressure and the three velocity components due to the wave motion were measured at a rate of 1 Hz during 1024 s every hour (every 1.5 h for the Chipehua station), while current measurements for the vertical profile were sampled every 20 min at 1.0 m cells within the water column (average during 90 s). Surface wave directional spectra were then estimated through standard direct Fourier transform routines ([Longuet-Higgins et al. 1963](#); [Young 1994](#)).

Additionally, two sites with high frequency radar systems (Wellen Radar, WERA) were in operation during the field campaign period, in order to retrieve surface current and wave fields. WERA stations were located at  $16^{\circ}4.24' \text{ N}$  and  $95^{\circ}21.76' \text{ W}$  (Cangrejo, CAN), and at  $16^{\circ}12.94' \text{ N}$  and  $94^{\circ}51.16' \text{ W}$  (Santa María del Mar, STM). These phase array WERA systems operated at 16.3 MHz with a typical coverage range of 100 km. Surface current and wave fields can be retrieved every hour with a spatial resolution of approximately 1 km by 1 km ([Fig. 1](#)).

To complement the remote sensing data collected during this experiment, a series of consecutive sea-surface images were acquired through the advanced synthetic aperture radar (ASAR) onboard the European satellite ENVISAT. Three sets of four ASAR single-look complex images (each image covering an ocean surface of about 100 km by 100 km each), were acquired on February 26 from 0419 to 0420 UTC; March 2 from 1620 to 1621 UTC; and March 18 from 1617 to 1618 UTC (see the frames for those images closest to the coast from the first two dates in [Fig. 1](#)). Each set of images, therefore, covered a strip of approximately 100 km wide by 400 km long of sea surface. The three sets (corresponding to 26 February 2005, 2 March 2005 and 18 March 2005) were acquired towards the end of *Tehuano* events (see [Sect. 3](#)).

### 3 Results

#### 3.1 Overall Wind Conditions

Prevailing wind conditions during the field campaign were typical for the Gulf of Tehuantepec winter season. At least eight *Tehuano* events were present and maximum wind speed (average over 30 min) was between  $10$  and  $19 \text{ m s}^{-1}$  (see [Fig. 2](#)). These events are defined here from the wind onset until the final wind fall. Therefore, low wind conditions are also included at the beginning and the end of each *Tehuano* event as can be observed in [Fig. 2](#). Wind direction during these events is persistently southwards, while it varies between events when wind speeds are lower than  $5 \text{ m s}^{-1}$ . In some cases moderate wind blowing northwards (not associated with *Tehuano* events) was observed (during day 58, for instance). It is interesting to note that in most cases the wind direction shifts clockwise during the *Tehuano* event onset, remains rather constant during the strong wind period, then varies clockwise again when the wind speed decreases.

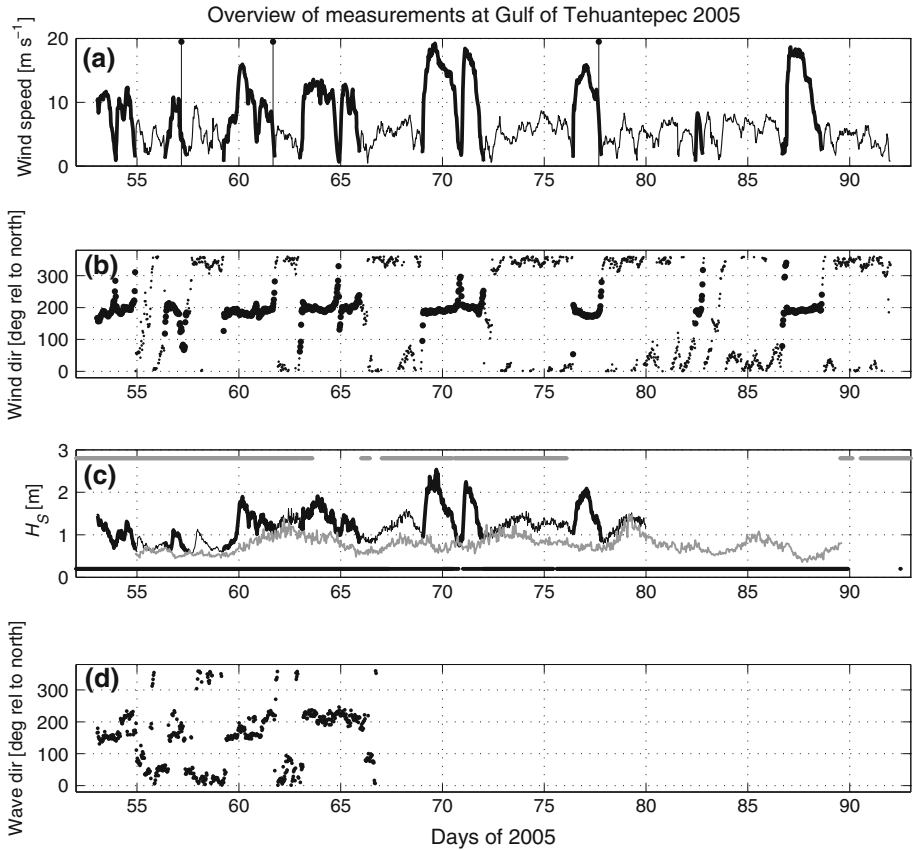


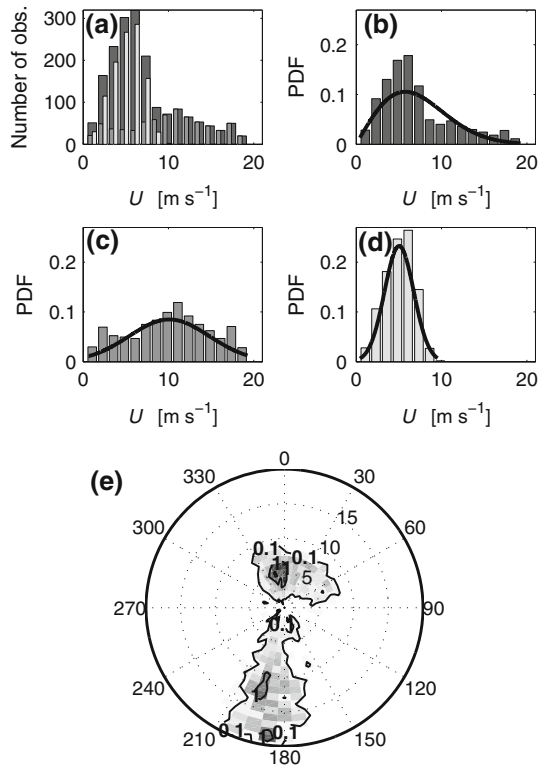
**Fig. 2** Overall mean conditions and overview of measurements in the Gulf of Tehuantepec during the INTOA experiment: (a) Wind speed and (b) wind direction (going to in degrees relative to north, oceanographic convention) as measured by the ASIS buoy at about 6.5 m above mean sea level. *Dark line and dots* depict the *Tehuano* events detected. Acquisition times for three sets of ASAR images are shown (*black dots and a vertical line*) in (a). (c) Significant wave height as measured by the ASIS buoy during *Tehuano* (*thick black lines*) and non-*Tehuano* (*thin line*) and by a Nortek acoustic Doppler current profiler near-shore (*grey line*) at Castillo station. *Horizontal lines* indicate the period of time when the high frequency radar systems (WERA) were in operation (*black: STM; grey: CAN*). (d) Spectral peak wave direction (going to in degrees relative to north, oceanographic convention) as inferred from the ASIS buoy measurements

In general terms, the total duration of *Tehuano* events detected varied from about 14 to 70 h. The onset time observed was between 5 and 19 h, although for most cases just about 6 h were required to reach maximum wind speed. Further details of these events, including start date and time, are given in Table 2. A characteristic sudden fall in wind speed in the middle of the event was observed in at least four of those events detected, showing wind speeds as low as  $1 \text{ m s}^{-1}$ . These relaxation periods, which last for a few hours, have been already observed by Barton et al. (2009) at a location near to the ASIS buoy (Salina Cruz) site. Some statistical analysis results from the wind observations during the INTOA experiment are shown in Fig. 3. Frequency distributions of wind speed as well as their associated probability density functions are shown in Fig. 3a–d, while the joint distribution of wind speed and direction is provided in Fig. 3e. A composite of histograms is shown in Fig. 3a for

**Table 2** Characteristics of *Tehuano* events occurred during the INTOA field campaign in the Gulf of Tehuantepec in early 2005

Label	Start (UTC)	Duration (h)	Mean wind ( $\text{m s}^{-1}$ )	Maximum wind ( $\text{m s}^{-1}$ )
TE1	22 Feb 2005 0104	43.5	8.45	12.33
TE2	25 Feb 2005 0854	25	5.89	10.79
TE3	28 Feb 2005 0559	53.5	8.84	15.96
TE4	02 Mar 2005 2353	62.5	9.53	13.57
TE5	09 Mar 2005 0017	70	12.91	19.26
TE6	16 Mar 2005 0955	33	11.61	15.89
TE7	22 Mar 2005 1013	14	5.17	8.33
TE8	26 Mar 2005 1633	45.5	11.98	18.66

**Fig. 3** Statistical results for wind measurements during the INTOA experiment. **(a)** Wind speed distribution for the total amount of observations (*black bars*), for exclusively *Tehuano* events (*grey bars*), and for non-*Tehuano* events (*white bars*). Wind-speed probability density functions (PDF) for **(b)** the total amount of data with a fitted Rayleigh distribution curve, **(c)** exclusively *Tehuano* events data, and **(d)** exclusively non-*Tehuano* data. A Gaussian distribution is fitted to the selected datasets **(c)** and **(d)**. PDFs are estimated in each case with reference to the total number of points in each selected dataset **(b)**, **(c)**, and **(d)**. **(e)** Joint distribution of wind speed and direction. Wind direction (in degrees) is measured clockwise relative to north (oceanographic convention). *Dotted circles* are wind speed measured from the centre in  $\text{m s}^{-1}$ . *Grey tones and contours* (0.1 and 1.0) correspond to the percentage of occurrence relative to the total number of observations



the total amount of wind speed data (black bars), for exclusively *Tehuano* event winds (grey bars), and for non-*Tehuano* winds (white bars). It can easily be seen that all cases with wind speeds  $>10 \text{ m s}^{-1}$  are due to *Tehuano* events.

For the period of our measurements, the probability density function (PDF) for the total amount of wind speed data resembles a Rayleigh distribution with  $6 \text{ m s}^{-1}$  as the most frequent speed (see Fig. 3b) and a parameter  $b = 5.7$  as obtained from the fitting procedure. *Tehuano* events wind speed distribution is observed as rather wide compared with the total distribution. Furthermore, relative maxima can be depicted at low ( $2 \text{ m s}^{-1}$ ), moderate ( $11 \text{ m s}^{-1}$ ),

and high ( $17 \text{ m s}^{-1}$ ) wind speeds (see Fig. 3c). It is readily apparent from Fig. 3d that the frequency distribution of exclusively non-*Tehuano* winds is well approximated by a Gaussian curve (with fitting parameters  $\mu = 5.0 \text{ m s}^{-1}$  and  $\sigma = 1.7 \text{ m s}^{-1}$ , where  $\mu$  is the mean and  $\sigma$  is the standard deviation). On the other hand, the frequency distribution of exclusively *Tehuano* winds is rather wide (see Fig. 3c), and a Gaussian fit ( $\mu = 10.1 \text{ m s}^{-1}$ , and  $\sigma = 4.7 \text{ m s}^{-1}$ ) seems to be only marginally better than a uniform distribution. From the wind speed and direction joint distributions shown in Fig. 3e, it can be seen that winds blowing offshore are practically concentrated towards  $190^\circ \pm 20^\circ$  (these are definitely *Tehuano* events since they are considered as winds blowing southwards). This characteristic and persistent wind direction makes this field site very distinctive. For this case, the two more important relative maxima are clearly depicted at moderate ( $11 \text{ m s}^{-1}$ ), and high ( $17 \text{ m s}^{-1}$ ) wind speeds (already shown in Fig. 3c). This joint distribution also shows a different regime corresponding with non-*Tehuano* northward wind conditions with typical speeds of about  $5 \text{ m s}^{-1}$ . It is also noticeable that winds blowing northwards were not detected with speeds higher than  $10 \text{ m s}^{-1}$ .

### 3.2 Wave Field Characteristics

The wave field in the Gulf of Tehuantepec can be described by the presence of a complex sea state, typically a combination of wind-sea and swell, where swell can be one or more systems. Swell generated by distant storms was present during the whole field campaign: while during non-*Tehuano* conditions it may follow, or propagate across the wind direction, during *Tehuano* events it always opposes the wind, particularly in the 100 km closest to the coast (it will be shown that swell travelling to the south-east was detected further offshore, in more open waters, through ASAR images of the sea surface).

Locally generated waves during *Tehuano* events were observed with  $H_S$  as high as 2.5 m as measured by the ASIS buoy (Fig. 2c), approximately 20 km offshore. The same winds however, are known to generate higher waves further offshore. The presence of swell over the whole measuring period is very characteristic. Swell significant wave height ( $H_{S_{swell}}$ ) varied from somewhat less than 0.5 m to about 1.5 m, as detected by a sensor near-shore (Fig. 2c).

Our analysis is focused on the wave field evolution for complex sea states, when locally generated wind-sea runs into long swell approaching the region from the opposite direction. Swell conditions have been conveniently classified according to the  $H_{S_{swell}}$  values. We refer to low significant wave conditions when  $H_{S_{swell}} < 0.5 \text{ m}$  on average, moderate conditions for values between 0.5 and 1.0 m, while high significant wave conditions when  $H_{S_{swell}} > 1.0 \text{ m}$ .

Time series of wave frequency spectra are shown in Fig. 4. For the case of wave spectra obtained from the measurements near-shore (Fig. 4a), the time evolution of the wave field shows essentially the swell signal. Arrival of shorter swell (higher frequencies) as time goes by can be readily seen, showing the classical dispersion process when waves propagate away from their source (distant storms). The presence of one or two (sometimes even three) swell systems at a particular time is also depicted. Practically most of the swell energy is encountered between 0.05 and 0.09 Hz frequency bands. Regarding the results from the ASIS buoy measurements (Fig. 4b), spectral energy density in the high frequency region is observed (typically for  $f > 0.2 \text{ Hz}$ ), specially when associated with the presence of strong *Tehuano* events. Relatively low to moderate spectral energy events are also observed with intermediate frequencies ( $0.10 \text{ Hz} < f < 0.15 \text{ Hz}$ ), between low-frequency long swell and high-frequency short locally-generated wind waves, which can be related to minor storms closer than those

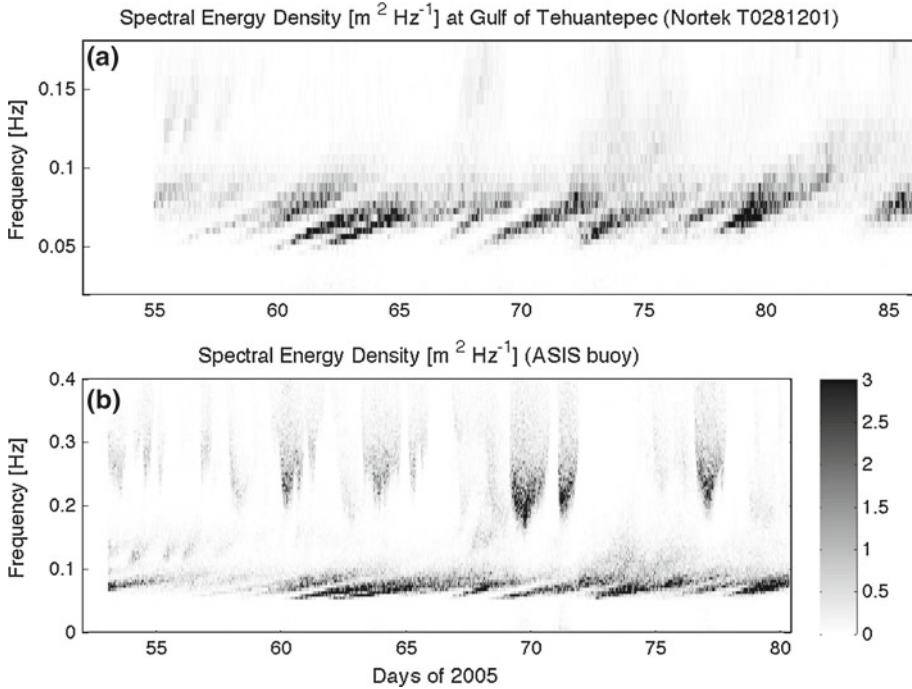


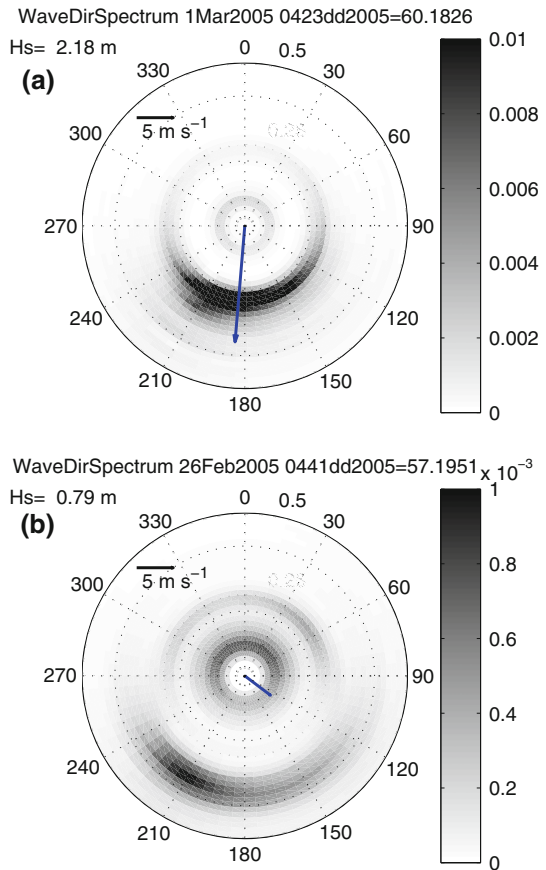
**Fig. 4** Time series of wave spectra (in  $\text{m}^2 \text{Hz}^{-1}$ ) as a function of frequency obtained from (a) measurements near-shore at Castillo Station (water depth is 20 m approximately), and (b) ASIS buoy (water depth about 60 m). Note the different frequency scale in order to better appreciate spectral energy features from each type of measurements

generating the longer swell. Ocean swell arrival and its variation as a function of time are also found at frequencies around 0.1 Hz and lower.

Wave energy density can also be represented in the form of the directional wave spectrum. Figure 5 shows typical directional wave spectra obtained from the ASIS buoy records. Figure 5a corresponds to 1 March 2005 at 0423 UTC (day of 2005  $dd = 60.1826$ ) for a particular case when a *Tehuano* event (TE3) occurred, with offshore winds of over  $15 \text{ m s}^{-1}$  (note the arrow in the polar plot). Locally generated waves are readily apparent in the relatively high frequency region within the spectrum with higher energy density than that associated with the swell system. As expected for wind-wave conditions, this part of the spectrum shows a relatively wide directional spread.

The presence of more than one wave system was rather common during the experiment, and an example of a multi-peaked spectrum also derived from the ASIS buoy records is included in Fig. 5b. This particular case corresponds to 26 February 2005 0441 UTC (wind direction  $dd = 57.1951$ ) and closely matches the acquisition time of the first set of ENVISAT ASAR images described in Sect. 2. As can be seen in the figure, three different peaks of wave energy are present: the lower-frequency signals represent two swell systems propagating towards the north-east and north-north-east, respectively, while the most conspicuous wave system corresponds to high frequency waves (fossil wind-sea) propagating towards the south-south-west, originally generated by the *Tehuano* event TE2. Again, the arrow at the centre of the plot represents the collocated wind vector measured by the buoy. By measurement time, the wind speed had already decreased to low values and the corresponding

**Fig. 5** Ocean surface wave directional spectra (in  $\text{m}^2 \text{Hz}^{-1}$ ) calculated from ASIS buoy measurements for (a) a particular time when a *Tehuano* event was on, and (b) a case when there were three wave systems detected while the preceding *Tehuano* wind was already relaxed. Direction is measured clockwise from north, while frequency is measured away from the plot origin up to a maximum of 0.5 Hz. Loci for 0.2 and 0.4 Hz are indicated (dotted circles). Wind-speed scale is shown with an horizontal arrow equivalent to  $5 \text{ m s}^{-1}$ . Note that the maximum in the spectral energy density scale in (b) is changed to  $1 \times 10^{-3} \text{ m}^2 \text{Hz}^{-1}$



locally generated waves were no longer noticeable at the buoy location. Rather, those high frequency waves still being observed represent a residual from the preceding *Tehuano* event (TE2) with their southward characteristic direction (associated with wind blowing towards  $200^\circ$  on average), shall not be, however, properly considered as wind-sea any longer.

Ocean surface waves might appear as distinct features on ASAR images, and different types of wave inversion algorithms have been proposed to derive integral parameters (Schulz-Stellenfleh et al. 2007) as well as the full directional (two-dimensional) spectrum (Schulz-Stellenfleh et al. 2005; Hasselmann and Hasselmann 1991), for the low-frequency region of the wave spectrum.

Some results from the analysis of ASAR images are shown in Fig. 6 to describe spatial variations of the wave field. The spatial distribution of wavelength and direction for the most important swell fields can be seen in Fig. 6a. The arrows are scaled with the swell wavelength and their orientation represent the direction of wave propagation. These characteristics associated with the swell spectral peaks were obtained from the spectral energy density estimated from an array of sub-images over the approximately 100 km by 400 km strip covered by one particular set of four ASAR images. Following the method presented in the study of Collard et al. (2005), each spectrum was estimated from a full resolution 512 by 512 pixels (12 km by 12 km approximately) sub-image. One swell system travelling south-eastwards is depicted only in the lower part of the imaged area (light grey arrows), while the most important swell

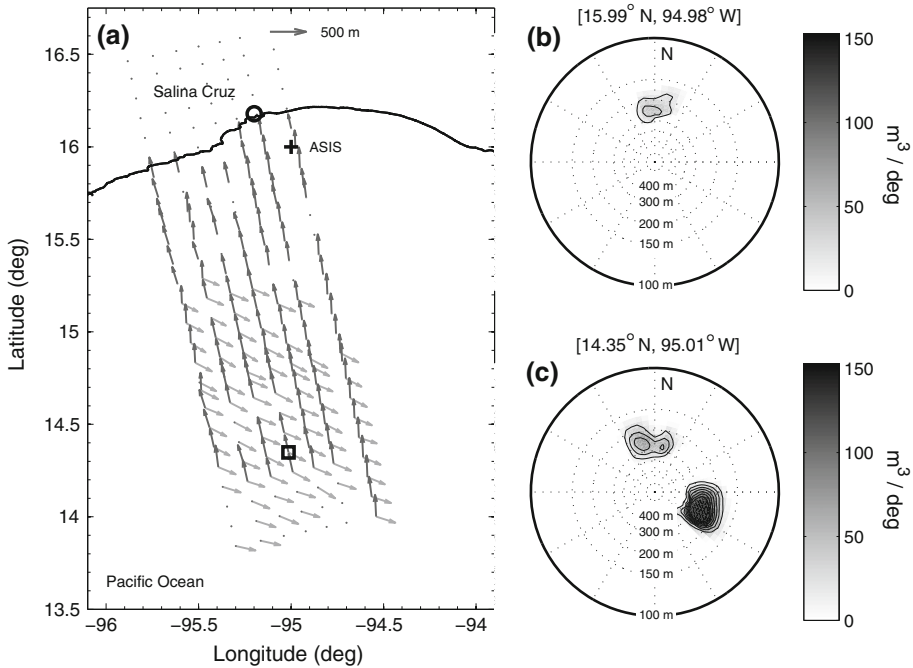


**Fig. 6** Description of the wave field in the Gulf of Tehuantepec as estimated from ASAR images acquired on February 26 from 0419 to 0420 UTC during the INTOA experiment. **(a)** Propagation direction and wavelength associated with two swell systems for the area covered by the set of four ASAR images. One swell system is propagating northwards (*dark grey arrows*) and another one propagating towards east-south-east (*light grey arrows*). Length of *arrows* are scaled with the swell wavelength in m (see *reference arrow* at the figure top corresponding to 500 m in length). Location for the ASIS buoy is indicated with a *plus sign*. Directional wave spectra estimated from sub-images **(b)** close to the ASIS buoy location and **(c)** at an offshore location (open square in **a**), are shown as a function of wavenumber and direction. Loci for reference wavelengths (400, 300, 200, 150 and 100 m) are shown as *dotted circles*. Evolution of the swell spectrum from the offshore location to near-shore at the ASIS buoy location is readily apparent

travelling northwards is shown practically over the whole area (dark grey arrows) in Fig. 6a. Both systems show wavelengths of about 260 m on average, with a main propagation direction of 115° and 350°, respectively. Dots without an arrow indicate locations of sub-images where the signal-to-noise ratio was insufficient to invert the spectrum properly, and so no wave information is retrieved.

Directional wave spectra (energy density as a function of wavenumber  $k$  and direction) from a sub-image very close to the ASIS buoy location are shown in Fig. 6b, and from a sub-image from the lower part of the figure (open square) in Fig. 6c. Some evolution of the swell spectrum associated with its propagation to shore can readily be noticed. An offshore two-peak swell spectrum with northwards propagation is modified to a simpler and somehow more concentrated spectrum in shallower waters closer to the coastline, at the particular location of the ASIS buoy. The swell part of the ASIS buoy directional spectrum already shown in Fig. 5b compares reasonably well with that presented in Fig. 6b (only waves of approximately 100 m wavelength or longer can be detected by the ASAR system). While the spectral peak wavelength is about 260 m from the ASAR wave spectrum, the frequency associated with the spectral peak from the ASIS buoy directional spectrum is 0.8 Hz approximately. Considering a depth equal to 60 m for the ASIS buoy location, through simple linear wave theory

an estimate of the associated wavelength is approximately 230 m, somewhat shorter than that estimated from the ASAR images. Although the main wave direction is rather similar towards 350° in both cases, estimates from the buoy measurements are directionally wider than the corresponding ASAR wave spectrum.

The swell propagating south-eastwards is only discernible offshore since (central-south) mainland Mexico plays an obstructing role to this type of wave field arriving from the North Pacific. In general terms,  $H_S$  values were about 0.6 m on average and its spatial variability analysis is still pending. Comparatively, results from the 2 March images suggest that only one swell system was present during the acquisition time. For this case, the wavelength was about 290 m on average, with an associated mean propagation direction of 350° approximately (towards the north-north-west), and mean  $H_S \approx 1.3$  m.

Regarding locally generated waves, it can be seen that the wind-sea exhibits different behaviour depending on wave maturity, which is characterised here through the wave age ( $C_p/U_{10}$ ) as underdeveloped ( $C_p/U_{10} < 1$ ) and developed waves ( $C_p/U_{10} \geq 1$ ). Wind-sea significant wave height ( $H_{S_{sea}}$ ) and spectral peak wavelength ( $\lambda_{P_{sea}}$ ) are plotted versus wind speed in Fig. 7. For this analysis in particular, wind speed is converted to a 10 m reference height, considering a neutrally stable atmosphere (see Sect. 3.3). As would be expected, observed developed wind waves (circles) are higher and longer than underdeveloped waves (up and down triangles) for any given wind speed. Developed waves closely follow the Pierson-Moskowitz description (solid line) for fully developed seas (Komen et al. 1984) indicating that observed developed waves are indeed fully developed during the experiment. In contrast, according to Kahma and Calkoen (1996) the underdeveloped waves (dashed line) grow at a lesser rate with increasing wind speed. However, significant wave height and wavelength of the observed underdeveloped waves being generated by winds blowing southwards are consistently lower and shorter than those predicted with the Kahma and Calkoen (1996) relation. It is believed that this difference is caused by the presence of swell (García-Nava et al. 2009). It is important to point out that in Fig. 7, both up and down triangles represent underdeveloped waves. The distinction however, is associated with the uncertainty regarding their underdevelopment. Up triangles correspond to waves being forced by winds blowing southwards ( $180^\circ \pm 30^\circ$ ). These conditions are identified as fetch-limited growth, with a fetch of about 22 km. Down triangles, however, correspond to those waves being forced by winds blowing mostly northwards, for which no information on fetch is available, therefore the growth might be either fetch- or duration-limited.

### 3.3 Momentum Flux and the Drag Coefficient

From wind velocity components measured by the sonic anemometer onboard the ASIS buoy, the wind stress ( $\hat{\tau}$ ) can be directly calculated through the eddy-correlation method as

$$\hat{\tau} = -\rho \left( \overline{u'w'}\hat{i} + \overline{v'w'}\hat{j} \right), \tag{1}$$

where  $u'$ ,  $v'$ , and  $w'$  are the turbulent velocity components,  $\rho$  is the air density and the overbar represents time averaging over 30 min. The sign is such that  $\hat{\tau}$  is in the direction of the horizontal velocity vector for a downward flux. The wind friction velocity ( $u_*$ ) can be directly estimated as  $u_* = [|\hat{\tau}|/\rho]^{1/2}$ .

Wind stress is typically expressed in terms of the drag coefficient,  $C_D$ , by

$$|\hat{\tau}| = \rho C_D U_z^2, \tag{2}$$

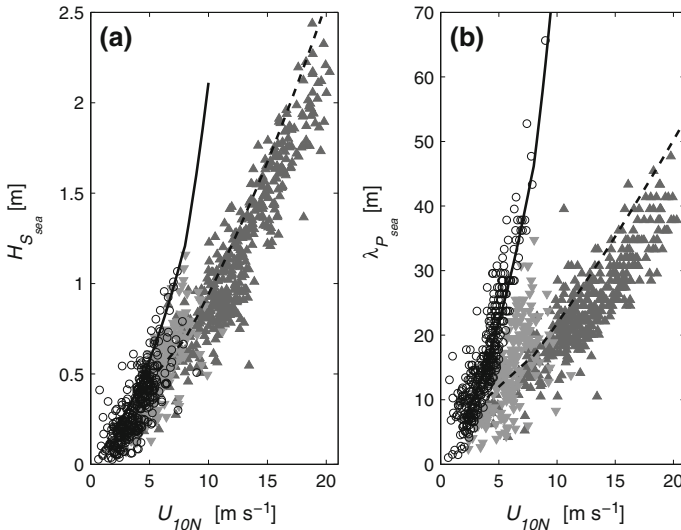


**Fig. 7** Description of wind-sea growth in terms of (a) its significant wave height ( $H_{S_{sea}}$ ), and (b) its spectral peak wavelength ( $\lambda_{P_{sea}}$ ), versus wind speed. *Circles* represent developed waves, *up triangles* underdeveloped waves from winds blowing southwards, and *down triangles* underdeveloped waves from winds blowing mostly northwards. *Lines* describe wave characteristics associated with Pierson-Moskowitz spectrum for fully developed seas (*solid*) and from the relationship given in the study by Kahma and Calkoen (1996) for fetch-limited wave growth (*dashed*)

and to avoid a dependance of  $C_D$  on measuring height and atmospheric stability,  $C_D$  was computed for neutral conditions at the 10 m standard height. Wind speed was converted to neutral conditions value using the flux profile relation (Donelan 1990)

$$U_{zN} = U_z + \frac{u_*}{\kappa} \psi_u, \tag{3}$$

where  $\kappa$  is the von Kármán constant,  $\psi_u = \psi_u(z/L)$  represents the non-dimensional gradient suggested by Donelan (1990), and  $L$  is the Obukhov length. Wind speed at standard 10 m height was then calculated assuming a logarithmic wind profile

$$U_{10N} = U_{zN} + \frac{u_*}{\kappa} \log \frac{10}{z} \tag{4}$$

and the drag coefficient directly determined through Eq. 2.

The neutral drag coefficient at 10 m height ( $C_{D_{10N}}$ ) is plotted as a function of wind speed ( $U_{10N}$ ) in Fig. 8. Single values of  $C_{D_{10N}}$  for each 30 min are represented by dots, while diamonds are the average of  $C_{D_{10N}}$  within wind-speed bins of  $1 \text{ m s}^{-1}$ , and error bars represent one standard deviation of the variation of  $C_{D_{10N}}$  within each wind-speed bin. For visual purposes all data points from the first bin (mean  $C_{D_{10N}} = 9.7 \times 10^{-3} \pm 6.9 \times 10^{-3}$ ) and four data points from the second bin were excluded from the graph. It can be seen that the drag coefficient tends to decrease with wind speed from low wind up to  $7 \text{ m s}^{-1}$  whereas for higher winds there is a linear increase and reduced scatter. The best fit for  $C_{D_{10N}}$  as a function of wind speed is:

$$C_{D_{10N}} = 1 \times 10^{-3} \begin{cases} 1 + 2.7U_{10N}^{-1} + 4.1U_{10N}^{-2} & U_{10N} \leq 7 \text{ m s}^{-1} \\ 0.73 + 0.083U_{10N} & U_{10N} > 7 \text{ m s}^{-1} \end{cases} \tag{5}$$

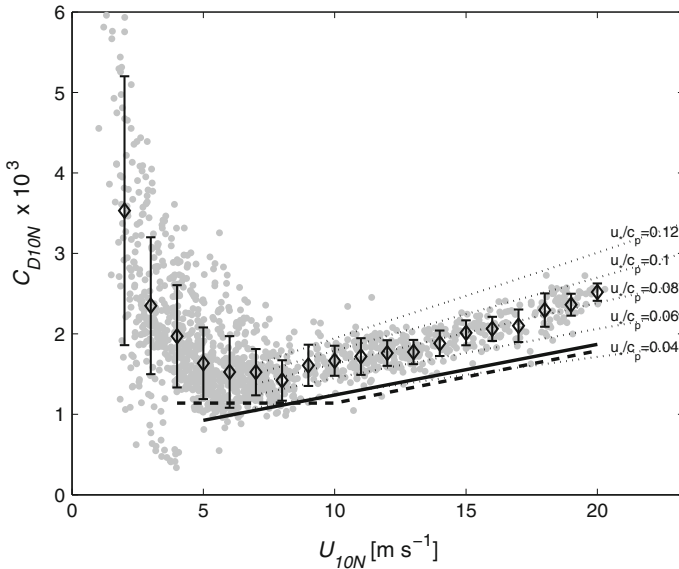


**Fig. 8** Drag coefficient from observations in the Gulf of Tehuantepec as a function of neutral wind speed. *Dots* represent data values for each 30 min, *diamonds* are the average  $C_{D10N}$  within wind speed bins of  $1 \text{ m s}^{-1}$  and the error bars are one standard deviation of  $C_{D10N}$  within each wind speed bin. The linear relations represent the expected  $C_{D10N}$  from [Smith \(1980\)](#) (*solid*) and [Large and Pond \(1981\)](#) (*dashed*); and from constant wave-age values using the [Drennan et al. \(2003\)](#) relation for pure wind-seas (*dotted*)

Observed  $C_{D10N}$  values are consistently higher than those reproduced from commonly used relationships such as those obtained from open ocean when rather well developed sea states were encountered ([Smith 1980](#); [Large and Pond 1981](#)).

For the particular cases of low wind conditions, the high drag coefficient values observed are probably caused by the presence of swell as previously documented by [Pan et al. \(2005\)](#) for similar conditions of offshore winds in the Gulf of Mexico and by [Donelan et al. \(1997\)](#).

A rather different regime prevails for moderate to high wind conditions ( $U_{10N} > 7 \text{ m s}^{-1}$ ), where almost all data (around 90%) correspond to northerly winds, i.e. offshore winds. Under these conditions, at the fixed fetch of the buoy location (22 km), wind generated waves are underdeveloped and they are even younger for higher wind speeds. Using a carefully selected dataset from several field experiments, [Drennan et al. \(2003\)](#) showed that for a pure wind-sea, the sea-surface roughness ( $z_0$ ) increases with the wave age (defined as the ratio between the friction velocity and the phase speed of the wind sea peak frequency,  $u_*/C_p$ ). Under neutral conditions there is a unique relationship between the surface roughness and the drag coefficient

$$C_{DzN} = \kappa^2 [\log(z/z_0)]^{-2} \tag{6}$$

hence, discussion may be either in terms of  $z_0$  or  $C_D$ . In [Fig. 8](#) dotted lines represent the  $C_{D10N}$  associated with the indicated wave age constant values, according to [Drennan et al. \(2003\)](#) relationship. It seems that the observed  $C_{D10N}$  for moderate to high wind speeds might be better represented by a relatively constant wave age  $u_*/C_p \approx 0.08$ , although in reality the wind-sea wave age increased linearly with wind speed and ranked, on average, from 0.05 at  $7 \text{ m s}^{-1}$  to 0.125 at  $20 \text{ m s}^{-1}$  as obtained from our measurements. Corresponding values of  $C_{D10N}$  for observed wave age calculated using the [Drennan et al. \(2003\)](#) pure wind-sea

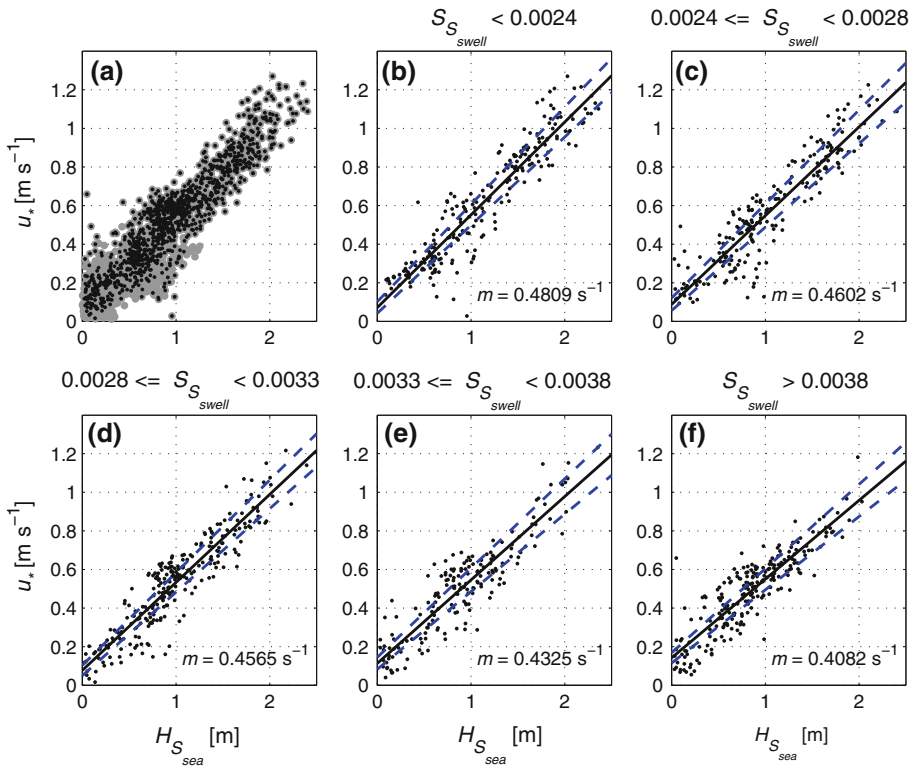


**Fig. 9** Results for the analysis regarding the relation between the sea state and the friction velocity ( $u_*$ ). Wind-sea representing the sea state is given by the significant wave height of locally generated waves ( $H_{S, \text{sea}}$ ). (a) All data points (grey dots) and those from the characteristic *Tehuano* events are shown (black dots). Sorted data with significant steepness of swell ( $S_{S, \text{swell}}$ ) varying from less than 0.0024 to more than 0.0038 are shown for (b)  $S_{S, \text{swell}} < 0.0024$ , (c)  $0.0024 \leq S_{S, \text{swell}} < 0.0028$ , (d)  $0.0028 \leq S_{S, \text{swell}} < 0.0033$ , (e)  $0.0033 \leq S_{S, \text{swell}} < 0.0038$ , and (f)  $S_{S, \text{swell}} > 0.0038$ . The slope (values given as variable  $m$  in each plot) of the regression lines (solid lines) gradually decreases as the significant steepness of swell increases from (b) to (f). The 95% confidence limits for the regression analysis are indicated by the dashed lines

relation are higher than those observed (not shown). It is worth to mention that the presence of swell can mask the relationship between wave age and surface roughness (Drennan et al. 2005). Swell is practically always present over the study period, then the relationship derived by Drennan et al. (2003) is used here only as a reference for what would be expected in the absence of swell, i.e. in pure wind-sea conditions. We therefore advance the hypothesis that the presence of swell somehow reduces the wind sea roughness, hence  $C_{D10N}$ . Observed drag coefficient in moderate to high wind conditions will correspond to  $C_{D10N}$  associated with young waves that do not reach a hypothetical pure wind-sea roughness value mainly due to the influence of the background swell. Further description of this matter is already dealt with in García-Nava et al. (2009). Focusing on the relevance of the sea state, rather than the wind speed alone, a different point of view allows us to detect a clear relationship of the wind stress as a function of the wind-sea significant wave height ( $H_{S, \text{sea}}$ ) as is shown in Fig. 9a. Dark dots represent data for *Tehuano* winds only, while grey dots are for all wind conditions.

Furthermore, in order to look in detail at the possible influence of swell, significant swell steepness ( $S_{S, \text{swell}}$ ) is calculated for each run of data and used to sort wind-sea significant wave height and the direct measurement of the wind stress (in terms of  $u_*$ ) for the *Tehuano*

**Table 3** Results for the linear regression analysis of data presented in Fig. 9

Case	$S_{S_{swell}}$ interval	$N$	$m$ ( $s^{-1}$ )	$m_{err}$ ( $s^{-1}$ )	$r$
(b)	$S_{S_{swell}} < 0.0024$	226	0.4809	$\pm 0.0239$	0.9353
(c)	$0.0024 \leq S_{S_{swell}} < 0.0028$	204	0.4602	$\pm 0.0273$	0.9193
(d)	$0.0028 \leq S_{S_{swell}} < 0.0033$	250	0.4565	$\pm 0.0237$	0.9232
(e)	$0.0033 \leq S_{S_{swell}} < 0.0038$	179	0.4325	$\pm 0.0302$	0.9048
(f)	$S_{S_{swell}} > 0.0038$	230	0.4082	$\pm 0.0282$	0.8836

The interval for the swell significant slope ( $S_{S_{swell}}$ ) is indicated as well as the number of data points ( $N$ ) for each case. Value for the regression line slopes are  $m$  and their corresponding error ( $m_{err}$ ) associated with 95% confidence limits, and correlation coefficient ( $r$ ) are also given

wind cases. Significant swell steepness is defined as the ratio between swell significant wave height and the wavelength associated to the swell spectral peak. In Fig. 9, the relation between  $u_*$  and the wind-sea significant height ( $H_{S_{sea}}$ ) is shown for various ranges of significant swell steepness. The slope of the regression lines gradually decreases in a consistent fashion as the significant swell steepness increases (see values for  $m$  in each plot). The errors ( $m_{err}$ ) associated with the estimated slope (with 95% confidence limits) of the regression line are only about 5% of the slope itself, and they are very similar in all five cases (see Fig. 9b–f), while the number of data points used varied from 179 to 250 (Table 3). This novel piece of information clearly indicates the influence of swell, inducing a reduced wind stress for  $H_{S_{sea}} > 1$  m, as the significant swell steepness ( $S_{S_{swell}}$ ) increased from values somewhat lower than 0.0024 to higher than 0.0038 (Fig. 9b–f). The range of  $S_{S_{swell}}$  encountered during the experiment corresponds to conditions of low to moderate swell, and it would be valuable to incorporate further measurements from steeper swell in a future analysis.

The distribution of friction velocity  $u_*$  and spectral peak phase speed for wind-sea encountered during the observations in the INTOA Experiment, is shown in Fig. 10. This provides us with an idea of the range of wave age experienced. Strictly speaking, no reference can be made to pure wind-sea cases, we rather document and stress the point of the underdeveloped conditions of the wind-sea regardless of the very common presence of swell. Cases for *Tehuano* events are identified as dark dots, while all the other cases are grey dots. Indication of underdeveloped waves are noticed for the limited-fetch growing conditions as from the characteristic offshore winds. The straight line defines  $C_{P_{sea}} = 20u_*$  typical for well-developed waves. It is also noticeable that for the wind-sea observed during *Tehuano* events, a wide range of development is detected, from well-developed seas for low  $u_*$  to very underdeveloped seas when extreme  $u_*$  was measured at the ASIS buoy location (with a fixed fetch).

## 4 Conclusions

The most important characteristics and overview of the INTOA Experiment have been presented, including an overview of the main characteristics of the study area and detailed information about *Tehuano* events. At least eight *Tehuano* events were detected, with a duration between 14 and 70 h, and wind speeds up to  $20 \text{ m s}^{-1}$ . During these *Tehuano* events the wind direction is very persistent and concentrated towards  $190^\circ$ . The wave field encountered is typically a combination of wind-sea and swell. The observed wind-sea exhibits different

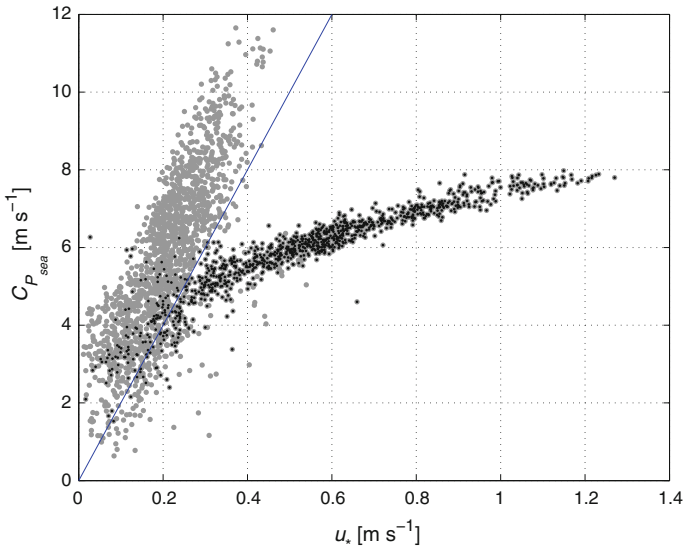


**Fig. 10** Distribution of friction velocity  $u_*$  and spectral peak phase speed for wind-sea encountered during observations in the INTOA Experiment, to provide an idea of the range of wave age. Cases for *Tehuano* events are identified as *dark dots*, while all the other cases are *grey dots*. Indication of underdeveloped waves are noticed for these limited-fetch growing conditions as from the characteristic offshore winds measured at the ASIS buoy specific location. The *straight line* defines  $C_{P_{sea}} = 20u_*$  typically for well-developed waves

behaviour depending on wave maturity or wave age. The significant wave heights and wavelengths of underdeveloped waves are consistently lower and shorter (respectively) than predicted with the [Kahma and Calkoen \(1996\)](#) relation. This difference between observed and predicted wave properties is believed to be caused by the presence of swell. Swell is present most of the time and can be composed of one or more systems. Locally generated waves were observed with  $H_S$  as high as 2.5 m as measured by the ASIS buoy, approximately 20 km offshore. The spatial variability of the swell systems present in the Gulf of Tehuantepec is studied through information retrieved from ASAR images and shows the evolution of the directional spectrum as well as that of wave-field integral parameters such as main wavelength and direction. The spatial variations described herein should be taken with caution since the observations are from an instantaneous point of view. A determination of momentum fluxes has been achieved through direct measurements with the ASIS buoy in the Gulf of Tehuantepec. Observed  $C_{D_{10N}}$  values are consistently higher than those reproduced from commonly used relations. Making use of the relationship derived by [Drennan et al. \(2003\)](#) as a reference (pure wind-sea relation), corresponding values of  $C_{D_{10N}}$  for observed wave ages are higher than those measured. It should be mentioned that the presence of swell might mask the original relationship between wave age and surface roughness. Nevertheless, it is shown what would be expected in the absence of swell (according to [Drennan et al. 2003](#)). Further analysis demonstrates a dependence of the wind stress on the sea state (wind-sea significant wave height). This dependence is then influenced by the significant swell steepness, consistently reducing the wind stress as the significant swell steepness increases. Although some influence of swell on the momentum fluxes has been presented in previous studies, this is the first time it is documented for the characteristic cases of swell

persistently and directly opposing offshore winds (*Tehuano* events) and the locally generated waves.

**Acknowledgments** The present work has been supported by CONACYT (62520, DIROCIOA), CICESE's Research Program for Wave Studies and UCMexUS-CONACYT (Collaborative Project Grant), while the INTOA experiment field campaign was supported by CONACYT (SEP-2003-C02-44718 and U40822-F). We thank all the technical personnel who contributed to the success of the experiment, particularly Joe Gabrielle, Mike Rebozo, Neil Williams and Sergio Ramos, and the officers and crew of DR06 Bahía Tepoca. The support provided by the Secretaría de Marina-Armada de México (Dirección General de Investigación y Desarrollo and Estación Oceanográfica de Salina Cruz) is greatly acknowledged. We are in debt to Pierre Flament for his contribution supplying electronic modules to operate two radar sites with 16 channels each. BOOST Technologies allowed us to use their software to retrieve the wave spectrum from ASAR images. Special thanks to Julieta Castro, Lina Zúñiga, and Mónica Sánchez for scientific activities co-ordination, logistic and administrative support. The final part of this work was developed during a sabbatical leave by FJO-T at ISMAR in Venice, with support from ICTP-TRIL Program, CONACYT (Programa de Estancias en el Extranjero) and CICESE. FJO-T would like to express his gratitude to Luigi Cavaleri and ISMAR staff for their support and hospitality. Anonymous reviewers are acknowledged for their interest and constructive comments.

## References

- Anctil F, Donelan MA, Drennan WM, Graber HC (1994) Eddy-correlation measurements of air-sea fluxes from a discuss buoy. *J Atmos Ocean Technol* 11:1144–1150
- Banner ML, Chen EJW, Walsh EJ, Jensen JB, Lee CS, Fandry C (1999) The southern ocean waves experiment, Part I, Overview and mean results. *J Phys Oceanogr* 29:2130–2145
- Barton ED, Lavín MF, Trasviña A (2009) Coastal circulation and hydrography in the Gulf of Tehuantepec, Mexico, during winter. *Cont Shelf Res* 29:485–500
- Collard F, Ardhuin F, Chapron B (2005) Extraction of coastal ocean wave fields from SAR images. *IEEE J Ocean Eng* 30:3. doi:[10.1109/JOE.2005.8575303](https://doi.org/10.1109/JOE.2005.8575303)
- Donelan MA (1990) Air-sea interaction. In: Méhauté BL, Hanes DM (eds) *The sea: ocean engineering science*, vol 1. Wiley, New York, 640 pp
- Donelan MA, Drennan WM, Katsaros K (1997) The air-sea momentum flux in conditions of wind sea and swell. *J Phys Oceanogr* 27:2087–2099
- Drennan WM, Donelan MA, Madsen N, Katsaros KB, Terray EA, Flagge CN (1994) Directional wave spectra from a swath ship at sea. *J Atmos Ocean Technol* 11:1109–1116
- Drennan WM, Kahma KK, Donelan MA (1999) On momentum flux and velocity spectra over waves. *Boundary-Layer Meteorol* 92:489–515
- Drennan WM, Graber HC, Hauser D, Quentin C (2003) On the wave age dependence of wind stress over pure wind seas. *J Geophys Res* 108(C3):8062
- Drennan WM, Taylor PK, Yelland MJ (2005) Parameterizing the sea surface roughness. *J Phys Oceanogr* 35:835–848
- Eymard L, Caniaux G, Dupuis H, Prieur L, Giordani H, Troadec R, Bessemoulin P, Lachaud G, Bouhours G, Bourras D, Guérin C, Le Borgne P, Brisson A, Marsouin A (1999) Surface fluxes in the North Atlantic during CATCH/FASTEX. *Q J Roy Meteorol Soc* 125:3563–3599
- García-Nava H, Ocampo-Torres FJ, Osuna P, Donelan MA (2009) Wind stress in the presence of swell under moderate to strong wind conditions. *J Geophys Res* 114:C12008. doi:[10.1029/2009JC005389](https://doi.org/10.1029/2009JC005389)
- Graber HC, Terray EA, Donelan MA, Drennan WM, Leer JCV, Peters DB (2000) ASIS-a new air-sea interaction spar buoy: design and performance at sea. *J Atmos Ocean Technol* 17:708–720
- Hasselmann K, Hasselmann S (1991) On the linear mapping of an ocean wave spectrum into a synthetic aperture radar image spectrum and its inversion. *J Geophys Res* 96:10713–10729
- Hauser D, Branger H, Bouffies-Cloché S, Despiou S, Drennan WM, Dupuis H, Durand P, Durrieu de Madron X, Estournel C, Eymard L, Flamant C, Graber HC, Guérin C, Kahma K, Lachaud G, Lefèvre J-M, Pelon J, Petterson H, Piguet B, Queffeuilou P, Tailliez D, Tournadre J, Weill A (2003) The FETCH experiment: an overview. *J Geophys Res* 108(C3):8053
- Kahma KK, Calkoen CJ (1996) Growth curve observations. In: Komen GJ, Cavaleri L, Donelan M, Hasselmann K, Hasselmann S, Janssen PAEM (eds) *Dynamics and modelling of ocean waves*. Cambridge University Press, Cambridge, 532 pp
- Komen G, Hasselmann S, Hasselmann K (1984) On the existence of a fully developed wind-sea spectrum. *J Phys Oceanogr* 14:1271–1285

- Large WG, Pond S (1981) Open ocean momentum flux measurements in moderate to strong winds. *J Phys Oceanogr* 11:324–336
- Longuet-Higgins MS, Cartwright DE, Smith ND (1963) Observations of the directional spectrum of sea waves using the motions of a floating buoy. In: *Ocean wave spectra*. Prentice-Hall Inc, Englewood Cliffs, 357 pp
- Pan J, Wang DW, Hwang PA (2005) A study of wave effects on wind stress over the ocean in a fetch-limited case. *J Geophys Res* 110:C02020. doi:[10.1029/2003JC002258](https://doi.org/10.1029/2003JC002258)
- Romero-Centeno R, Zavala-Hidalgo J, Gallegos A, O'Brien JJ (2003) Isthmus of Tehuantepec wind climatology and ENSO signal. *J Clim* 16:2628–2639
- Schulz-Stellenfleth J, Lehner S, Hoja D (2005) A parametric scheme for the retrieval of two-dimensional ocean wave spectra from synthetic aperture radar look cross spectra. *J Geophys Res* 110:C05004. doi:[10.1029/2004JC002822](https://doi.org/10.1029/2004JC002822)
- Schulz-Stellenfleth J, König T, Lehner S (2007) An empirical approach for the retrieval of integral ocean wave parameters from synthetic aperture radar data. *J Geophys Res* 112:C03019. doi:[10.1029/2006JC003970](https://doi.org/10.1029/2006JC003970)
- Smith SD (1980) Wind stress and heat flux over the ocean in gale force winds. *J Phys Oceanogr* 10:709–729
- Young IR (1994) On the measurement of directional wave spectra. *Appl Ocean Res* 16:283–294